Chinese Journal of Chemical Engineering 56 (2023) 242–254

Contents lists available at ScienceDirect

Chinese Journal of Chemical Engineering

journal homepage: www.elsevier.com/locate/CJChE

Full Length Article

Cracking and buoyancy effect on hydrocarbon endothermic and heat transfer characteristics in rectangular mini-channel

Chengang Yang, Huaizhi Han *, Quan Zhu, Xiangyuan Li

School of Chemical Engineering, Sichuan University, Chengdu 610065, China
Engineering Research Center of Combustion and Cooling for Aerospace Power, Ministry of Education, Sichuan University, Chengdu 610065, China

ARTICLE INFO

Article history:
Received 13 April 2022
Received in revised form 20 July 2022
Accepted 24 July 2022
Available online 28 July 2022

Keywords:
Heat transfer
Computational fluid dynamics (CFD)
Buoyancy
Hydrocarbons

ABSTRACT

Although buoyancy and cracking reactions are strongly coupled in the active cooling process, most of the previous studies consider only one of these factors, and their coupling relationship has not been considerably examined. In this work, this coupling relationship was numerically investigated with complete consideration of different cases of heating, and in the view of energy transport and conversion. By comparing with the no-gravity case (NGC), the results indicate that buoyancy has a significant effect on the bottom-heated case (BHC) and side-heated case (SHC), but has little influence on the top-heated case (THC) owing to the different magnitudes of secondary flow. The heat transfer of the BHC and SHC was significantly enhanced by the secondary flow, but their energy conversion was simultaneously impaired. The conversion of the BHC and SHC was approximately half that of the THC and NGC. For all cases, by analyzing the energy transport ways, the cross section can be classified into three regions in the heating direction. Laminar conduction dominates in region I, but gradually fails in region II, where its role is replaced by other energy transport ways. In region III, convection dominates the energy transport for BHC and SHC, whereas turbulence dominates for THC and NGC.

1. Introduction

Scramjet, the key component of hypersonic aircraft, can encounter an extremely high heat load owing to air friction and combustion [1,2]. Thus, it is critical to find an efficient and feasible cooling technology to keep the scramjet running steadily. The most promising cooling technology is active cooling, which uses fuel as the coolant to cool the combustion chamber of a scramjet [3]. However, this cooling process can be extremely complicated as it simultaneously includes flow, heat transfer, and cracking reaction, while fuel passes through the cooling channels inside the engine wall. Therefore, this complex coupling mechanism of the cooling process needs to be revealed to support the rational design of scramjets [4].

Overall, the flow, heat transfer, and cracking reactions in the active cooling process are highly coupled. Many experimental studies have indicated that the occurrence of cracking may improve the heat transfer and heat absorption [5,6], while variations in the flow and heat transfer states can also lead to different reaction characteristics [7,8]. However, by experimental methods, it is difficult to analyze the interaction mechanisms of flow, heat transfer, and cracking reactions. Therefore, numerical methods were developed to reveal the details and interaction mechanisms of these processes. In early studies, one of the obstacles to numerical model development is the modeling of the cracking reaction. From the perspective of elementary reactions, the cracking reaction includes hundreds of species and thousands of reaction paths [9] thus, modeling and solving the entire reaction network seems to be extremely difficult. Fortunately, Ward *et al.* [10,11] found that at low conversions, the product distribution of the cracking reaction is proportional, even in a wide pressure range. Therefore, at low conversion, the cracking reaction can be simplified to a one-step reaction, which makes it possible to incorporate the cracking reaction into the numerical model. Subsequently, based on the proportional product distribution assumption, a series of cracking reaction mechanisms for various hydrocarbon fuels have been proposed [12–15]. Moreover, a few reaction mechanisms that further considered secondary reactions have been developed in recent years [16–18]. These mechanisms can be applied under high-conversion conditions.

Owing to the progress in reaction modeling, massive numerical investigations have been conducted to reveal the joint effect of flow, heat transfer, and cracking reaction in the active cooling

* Corresponding author.
E-mail address: hanhz@scu.edu.cn (H. Han).

https://doi.org/10.1016/j.cjche.2022.07.024
1004-9541/

process. In general, 2D and 3D model is more frequently used in the numerical investigations than 1D model as large gradient exist in spanwise direction and this gradient has significant impact on cracking reaction and heat transfer [19]. These investigations indicated that the cracking of hydrocarbon fuel has a considerably positive effect on enhancing property uniformity at the cross section [20], and reducing the bulk and wall temperatures [21]. Meanwhile, the change in flow and heat transfer significantly influences the cracking reaction [8]. This coupling relationship varies under specific conditions. For instance, Feng *et al.* [22,23] suggested that according to the characteristic time variation, this coupling relationship can considerably change in both the axis and radial directions. Li *et al.* [24] indicated that high-degreed cracking reaction near side wall can increase the near-wall thermal resistances and thus impair the heat transfer. Furthermore, with the development of numerical models, further influencing factors in the active cooling process, such as pressure [25], rib [26], coking [27] and flow distribution [28,29] were taken into consideration.

Recently, it was recognized that a high heat flux in the active cooling process may induce a strong buoyancy effect. Therefore, many studies have attempted to determine the buoyancy effect. Buoyancy effect can be especially prominent in upward or downward flow. Zhu *et al.* [30] investigated the heat transfer in a vertical tube and found that the buoyancy effect is more significant in a large tube than in the small one. Sun *et al.* [31] indicated that upward flows and heat transfer in a vertical tube at supercritical pressures can be divided into three stages and corresponding characteristics of each stage was pointed out. Meanwhile, buoyancy also have significant effect for horizon flow. Sun *et al.* [32] found that, for rectangular tube, the drastic variation of fluid density can induce strong buoyancy effect and this buoyancy effect is highly relevant to the position of the heated wall. By analyzing turbulence characteristics and entropy generation, Sun *et al.* [33] indicated that buoyancy is strongly related to heat transfer and can change streamwise turbulent heat flux.

All the above studies exhibit the importance of buoyancy, however, none of them simultaneously consider the effect of cracking reaction. As indicated by previous research, cracking reactions can considerably change fuel properties [8,34] and fuel properties directly determine the buoyancy effect. Therefore, only by considering the cracking reaction, can the buoyancy effect in the active cooling process be comprehensively investigated.

In this work, a numerical model inclusively considering both these effects was constructed to determine the coupling relationship between the buoyancy effect and cracking reaction. The proportional product distribution (PPD) mechanism and real gas model were adopted to depict the cracking and property variations. Considering the influence of the heated wall location [32], all cases of bottom-heated case (BHC), side-heated case (SHC), and top-heated case (THC) were investigated and compared with the no-gravity case (NGC). The results were first analyzed to determine the basic physical quantities such as density, velocity, and temperature, and subsequent analysis was conducted to investigate the underlying mechanism of energy conversion and transport. The results of this work may provide helpful guidance for utilizing the positive effects of buoyancy and alleviating its negative effects.

2. Numerical Methods

2.1. Geometry and mesh

As shown in Fig. 1, a square channel was adopted in this study to represent a single cooling channel. The width and height of the cooling channel were 2 mm. As the present study focuses on the buoyancy effect on the fluid region, the surrounding solid region was not considered. To avoid the inlet and outlet effects, inlet and outlet sections with lengths of 100 mm were connected to the two ends of the heated section. The length of the heated section was set to 400 mm. A structured mesh was adopted to discretize the fluid domain. As property gradients dramatically vary from the near-wall region to the main flow region [23], the dramatic expansion of mesh elements was set to fit this variation.

2.2. Governing equations

The governing equations of continuity, momentum, energy, and species are numerically solved. All the equations are as follows:

Continuity equation:

$$\nabla \cdot (\rho \boldsymbol{U}) = 0 \tag{1}$$

Momentum equation:

$$\nabla(\rho \boldsymbol{U}\boldsymbol{U}) = -\nabla p + \nabla \tau + \rho \boldsymbol{g} \tag{2}$$

Energy equation:

$$\nabla \cdot [\boldsymbol{U}(\rho E + p)] = \nabla \cdot \left(\lambda \nabla T - \sum_i H_i \boldsymbol{J}_i \right) \tag{3}$$

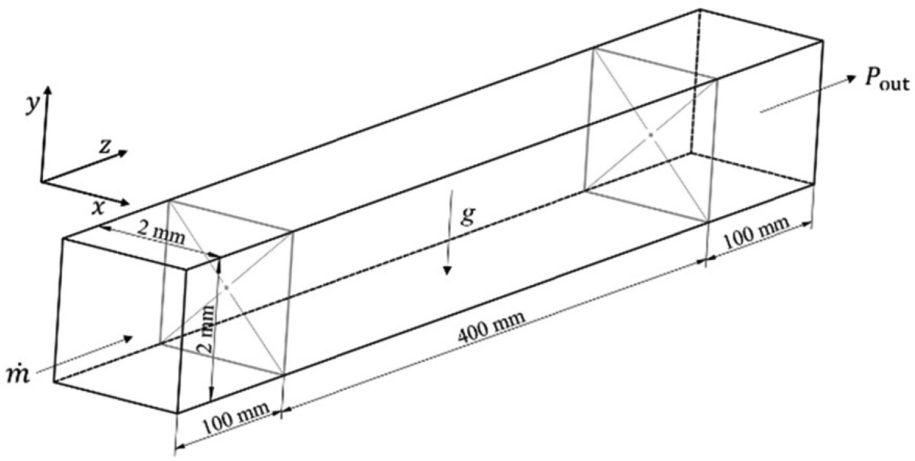

Fig. 1. Schematic of the cooling channel.

As the radiation heat flux only accounts for less than 3% of the total heat flux, it was neglected in the present study.

Species equation:

$$\nabla \cdot (\rho \boldsymbol{U} W_i) = -\nabla \cdot \boldsymbol{J}_i + r_i \tag{4}$$

As pointed out by Xu *et al.* [35], while the cracking reaction is considered, the SST k–ω model [36] has the best performance in predicting the wall temperature at $Re_{in} = 700$, which is very close to the present condition of $Re_{in} = 796$. Therefore, the SST k–ω model was adopted to handle the turbulence flow.

2.3. Cracking reaction model

As the temperature of the heated wall can reach approximately 1000 K, the cracking of hydrocarbons inevitably needs to be considered. To simplify the reaction modeling, it was assumed that the cracking products were proportionally distributed, as proposed by Ward *et al.* [10,11]. Therefore, the PPD model proposed by Qin *et al.* [12] was incorporated with the governing equations.

$$\begin{aligned} C_{10}H_{22} = {} & 0.151H_2 + 0.143CH_4 + 0.256C_2H_4 + 0.126C_2H_6 + \\ & 0.230C_3H_6 + 0.180C_3H_8 + 0.196C_4H_8 + \\ & 0.102C_4H_{10} + 0.171C_5H_{10} + 0.124C_5H_{12} + \\ & 0.195C_6H_{12} + 0.089C_6H_{14} + 0.169C_7H_{14} + \\ & 0.072C_7H_{16} + 0.152C_8H_{16} + 0.012C_8H_{18} + \\ & 0.053C_9H_{18} + 0.003C_9H_{20} \end{aligned} \tag{5}$$

The source term of the species equation can be expressed as:

$$r_i = M_{w,i} k C_{C_{10}H_{22}} \tag{6}$$

According to the Arrhenius equation, the rate constant of the cracking reaction can be expressed as:

$$k = A_0 \exp\left(-\frac{E_a}{RT}\right) \tag{7}$$

The values of A_0 and E_a proposed by Qin *et al.* [12] for 5 MPa are 1.7×10^{15} s^{-1} and 246.2 $kJ \cdot mol^{-1}$, respectively.

2.4. Thermophysical properties

The density of fuel was calculated according to the Peng–Robinson equation of state (PR EoS) because of its excellent performance in predicting hydrocarbon density [37].

$$p = \frac{RT}{V-b} - \frac{a(T)}{V(V+b)+b(V-b)} \tag{8}$$

$$a(T) = 0.45724 \frac{R^2 T_c^2}{p_c} \alpha(T) \tag{9}$$

$$b = 0.07780 \frac{RT_c}{p_c} \tag{10}$$

$$\alpha(T) = \left[1 + \left(0.37464 + 1.54226\omega - 0.26992\omega^2\right)\left(1 - T_r^2\right)\right]^2 \tag{11}$$

The specific heat capacity of fuel was calculated as follows:

$$c_p = c_p^0 - F_{dep} \tag{12}$$

$$c_p^0 = a_1 T^4 + a_2 T^3 + a_3 T^2 + a_4 T + a_5 \tag{13}$$

$$F_{dep} = T \int_V^\infty \left[\left(\frac{\partial^2 p}{\partial T^2}\right)_V\right]_T \mathrm{d}V + T\left(\frac{\partial p}{\partial T}\right)_V^2 \Big/ \left(\frac{\partial p}{\partial V}\right)_T + R \tag{14}$$

where c_p^0 indicates the ideal specific heat capacity, and it was fitted into a fourth-order function that depends on temperature. F_{dep} is a departure function that aims to correct the pressure influence.

The van der Waals mixing rule was adopted to calculate the EoS parameters of the cracked mixture:

$$(\alpha_m)^{0.5} = \sum_i^n x_i (\alpha_i)^{0.5} \tag{15}$$

$$b_m = \sum_i^n x_i b_i \tag{16}$$

The ideal specific heat capacity of mixture was calculated by molar fraction averaging:

$$c_{p,m}^0 = \sum_i^n x_i c_{p,i}^0 \tag{17}$$

The viscosity and thermal conductivity of the hydrocarbon mixture were calculated according to the method of Chung *et al.* [38].

The diffusivity of the hydrocarbon mixture was calculated in three steps: First, the binary diffusivity of gases at low pressure was calculated by an empirical correlation proposed by Fuller *et al.* [39]. Then, a correction proposed by Takahashi [40] was adopted to introduce the effect of pressure on the binary diffusivity. Finally, the overall diffusivity of the hydrocarbon mixture was calculated according to Blane's mixing law [41] as shown in Eq. (18).

$$\Gamma_i = \left(\sum_{\substack{j=1 \\ j \neq i}}^n \frac{x_j}{\Gamma_{ij}}\right)^{-1} \tag{18}$$

The calculation results of these thermophysical properties at 5 MPa are shown in Fig. 2. By comparing with the data of the National Institute of Standards and Technology (NIST), it can be concluded that the present methods are well suited for predicting the thermophysical properties such as density, specific heat capacity, viscosity, and thermal conductivity. Fig. 2 also indicates that the dramatic variation in properties of *n*-decane near the pseudo-critical region [42], where second-order phase transition [43] occurred, can also be well captured by the present methods. The average relative deviations of density, specific heat capacity, viscosity, and thermal conductivity were 6.5%, 2.2%, 7.3%, and 16.4%, respectively.

2.5. Boundary conditions

A mass flow inlet of $\dot{m} = 0.5$ $g \cdot s^{-1}$ with pure *n*-decane, and an outlet pressure of $p_o = 5$ MPa were set as the inlet and outlet boundary conditions. The inlet temperature of the hydrocarbon fuel was set to $T_{in} = 300$ K. A constant heat flux of $q = 1.0$ $MW \cdot m^{-2}$ was imposed on the heated wall, which could be the bottom wall, side wall, or top wall. Except for the heated wall, all the other three walls were set to be adiabatic.

2.6. Meshing independence

Three sets of meshes with dimensions of 60 × 600, 60 × 900, and 80 × 600 were compared to validate the grid independence. The y^+ of the first mesh layer is less than 1 to satisfy the requirements of the SST k–ω model. As shown in Fig. 3, while the grid number in the z-direction increased from 600 to 900, the relative difference of T_b along the channel was within 0.3%, and the relative difference of $W_{C_{10}H_{22}}$ was within 0.5%. Meanwhile, while the grid number in the x-and y-directions increased from 60 to 80, the rel-

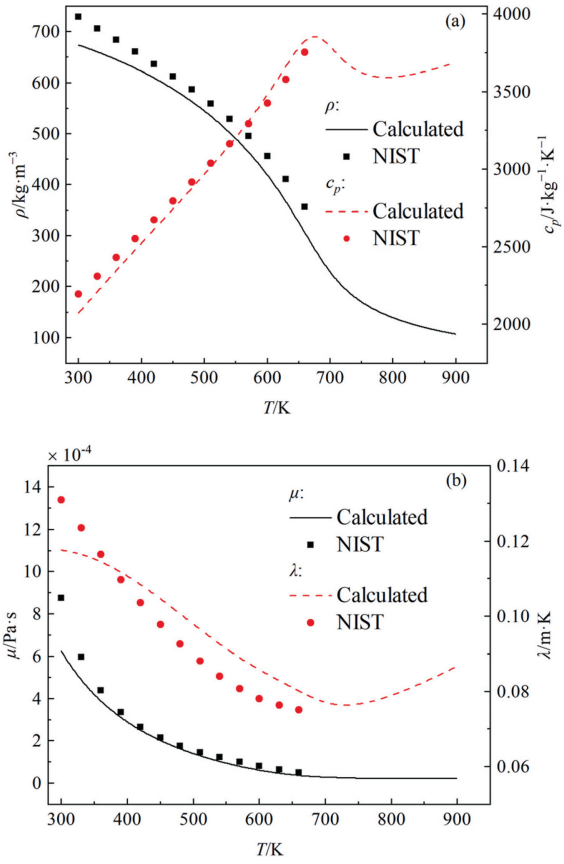

Fig. 2. Validation of the thermophysical properties of *n*-decane at 5 MPa.

ative difference of T_b along the channel was within 0.7%, and the relative difference of $W_{C_{10}H_{22}}$ was within 1.2%. Therefore, a mesh of 60 × 600 was sufficient to satisfy the computational accuracy, and was ultimately adopted in this study.

2.7. Model validation

To validate the present numerical model, two sets of experiments were conducted and compared with the corresponding simulation results. The conditions of the validation experiment are listed in Table 1. In accordance with the simulation geometry, a rectangular tube was adopted to validate the present numerical model. The height and width of the rectangular channel are 1.6 mm on the inside, and 3.0 mm on the outside. More details about the experimental facility and methods can be found in our previous research [8]. As shown in Fig. 4, both the outlet temperature and outlet mass fraction of *n*-decane in Case 1 could be predicted well by the present numerical model, where the relative deviations in the outlet temperature and mass fraction of *n*-decane are 0.74% and 1.4%, respectively. Meanwhile, it can be seen that these relative deviations in Case 2 can be enlarged as the heat flux increases and secondary reactions occur [12]. In Case 2, as the secondary reactions were not considered in Qin *et al.* mechanism, the relative deviation of the outlet temperature and mass fraction of *n*-decane could be increased to 0.62% and 11.9%, respectively. Because this study mainly focuses on the buoyancy effect on the energy transport and conversion process, this deviation is still acceptable.

3. Results and Discussion

3.1. Density and secondary flow

Density ρ, as the exclusive and direct influencing factor of the buoyancy effect, plays a significant role in the energy conversion and transport processes. Therefore, it is essential to analyze distribution of ρ in both the flow and heating directions.

$$\rho_{ave} = \frac{\int \rho dA}{\int dA} \tag{19}$$

The average ρ in the cross-section at D_z along the cooling channel was calculated using Eq. (19), and are presented in Fig. 5(a). For these four cases, ρ decreases slightly at first, then decreases rapidly as T_b approaches the pseudo-critical temperature, and subsequently decreases slightly again. For the BHC, while $D_z < 0.24$ m, ρ is slightly larger than that in the other three cases. However, with the increase in D_z, ρ of the SHC gradually becomes the largest. The values of ρ for THC and NGC are approximately the same in the

Table 1
Validation experiment conditions.

Case	Channel shape	T_{in}/K	$\dot{m}$/g·s^{-1}	$\dot{q}$/W·m^{-3}
1	Rectangular	300	0.94	2.8×10^8
2				3.4×10^8

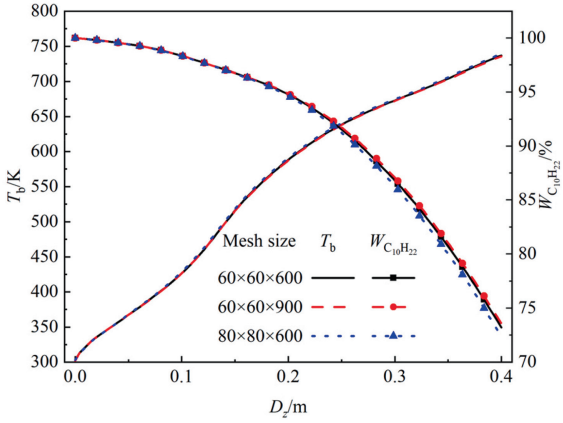

Fig. 3. Results of mesh independence.

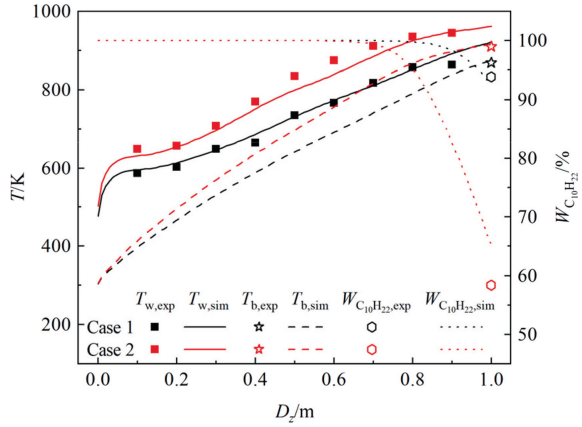

Fig. 4. Comparison between simulation and experimental results.

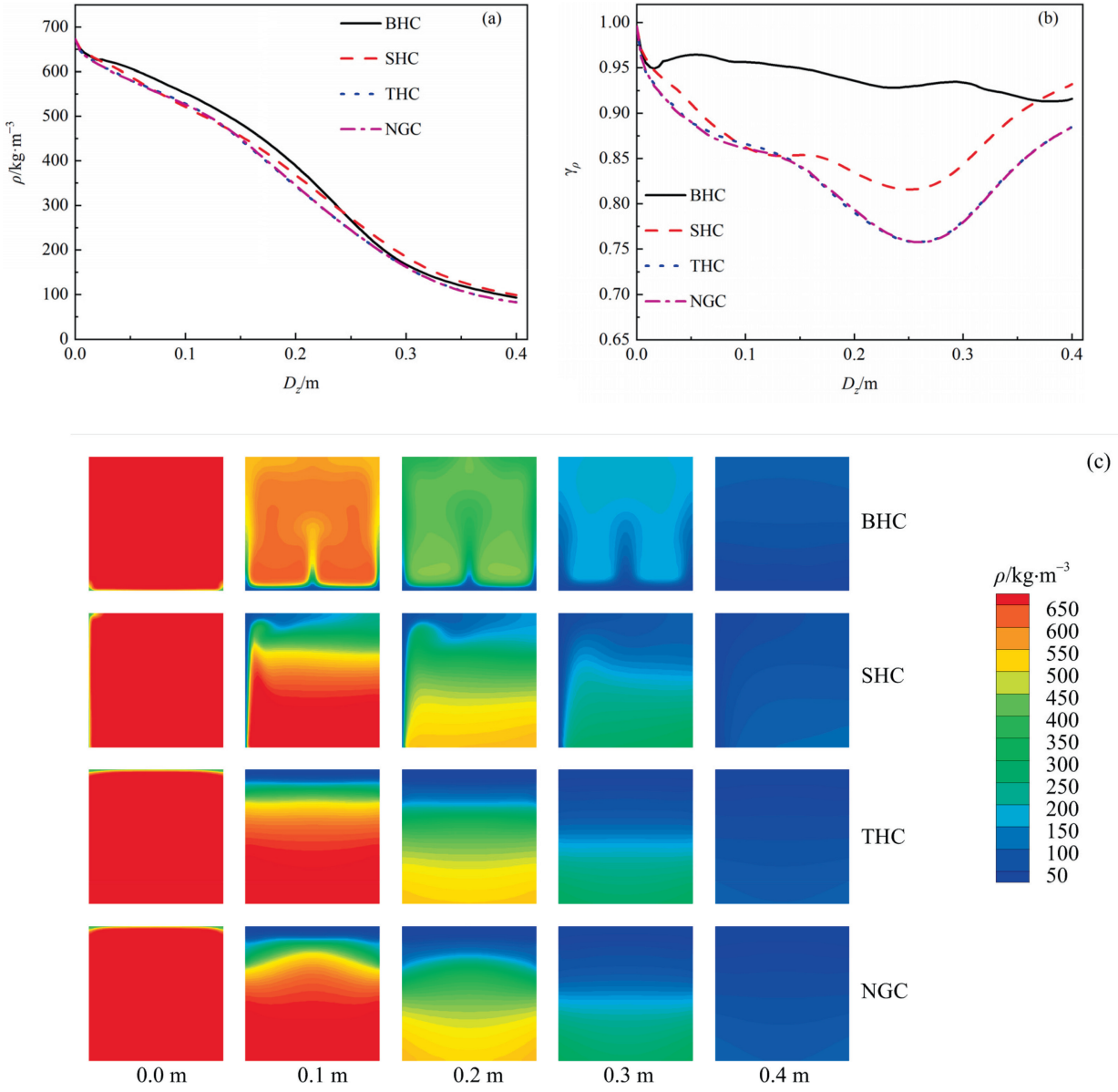

Fig. 5. (a) Density along the channel with different heated surfaces; (b) Density uniformity along the channel with different heated surfaces; (c) Density contours at different cross sections with different heated surfaces.

entire channel and are smaller than ρ of BHC and SHC. The difference in ρ distribution for these four cases is not large, and the maximum relative difference is only 16%.

According to several previous studies [44–47], the most significant factor influencing the buoyancy effect is density uniformity. Thus, it is necessary to quantify the density uniformity to determine the cause of different buoyancy effects induced in different cases. In this study, the uniformity of density γ_ρ in every cross section was defined in an area-weighted form, as shown in Eq. (20), and the corresponding results are presented in Fig. 5(b).

$$\gamma_\rho = 1 - \frac{\int |\rho - \rho_{ave}| dA}{2 \int \rho_{ave} dA} \tag{20}$$

where ρ_{ave} is the area-weighted average density in the cross section.

Clearly, BHC has the best density uniformity compared to that of the other cases. For BHC, the variation in γ_ρ is small compared with γ_ρ variation of the other three cases. The γ_ρ of SHC, THC, and NGC decreased in the first three quarters of the cooling channel and then recovered in the last quarter. The γ_ρ of SHC was better than that of THC and NGC.

To obtain further details, the ρ distributions in different cross-sections for these four cases are presented in Fig. 5(c). For all cases, a large ρ gradient could be observed near the heated wall. With an increase in the distance from the heated wall, an obvious difference in ρ profile can be seen for different cases. With the increase in D_z, for different cases, different density contours evolved because of the influence of gravity. For the BHC, with an increase in D_z, the lightweight fluid is gradually centralized at the center and two sides of the heated wall. Obvious stratification can be observed in the front section of the cooling channel. At the end of the channel, this phenomenon disappeared when the large density gradient was eliminated. For the SHC, with an increase in D_z, the cross section of the channel was divided into two regions: in the near-heated wall region, massive heat crossed the heated wall

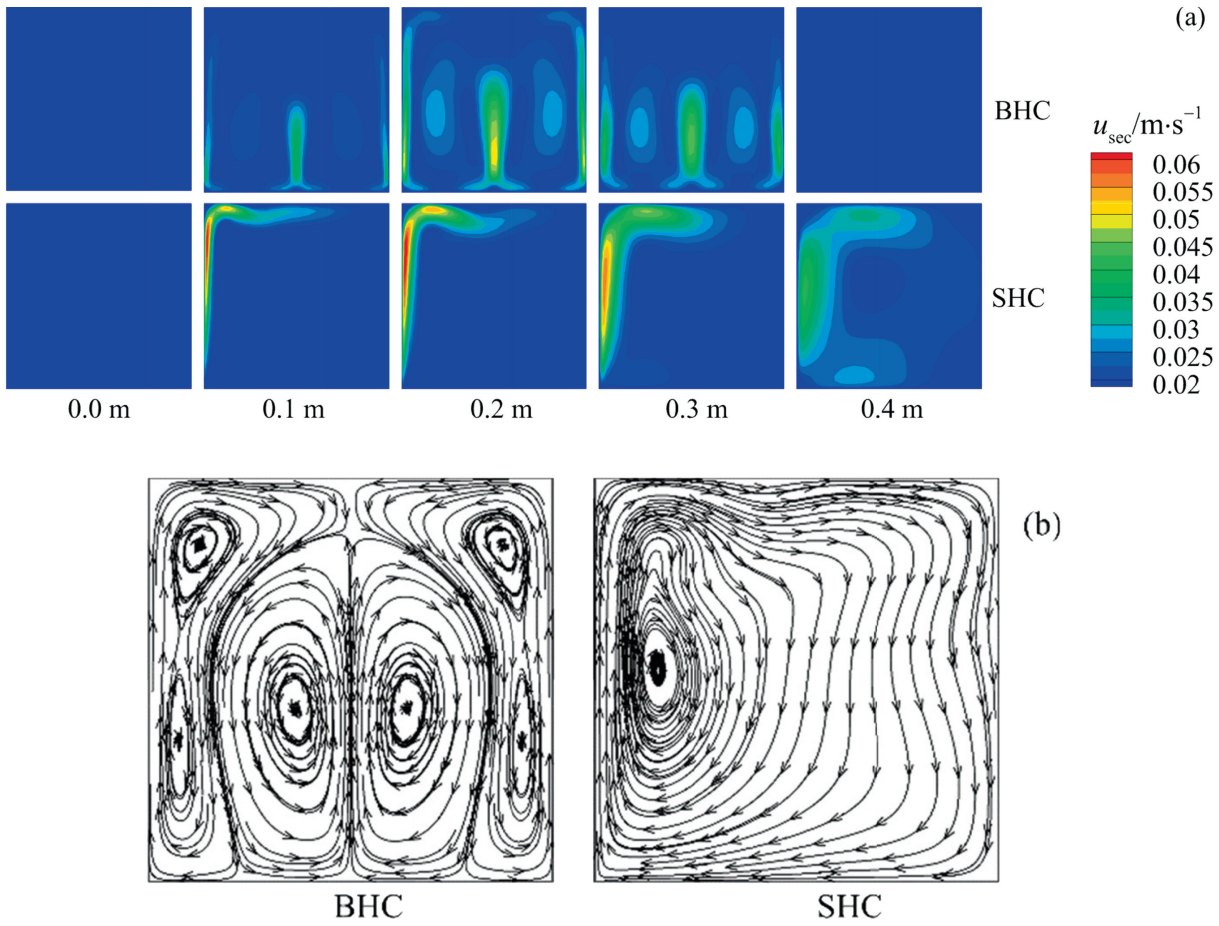

Fig. 6. (a) Secondary flow velocity contours at different cross sections for BHC and SHC; (b) Stream lines at the cross sections of $D_z = 0.3$ m for BHC and SHC.

and entered the fluid. Therefore, a thermal boundary was formed, and strong stratification parallel to the heated wall could be seen in the near-heated wall region. Then, driven by gravity, the lightweight fluid floats up to the top and heavy fluid sinks to the bottom. Because of the obstruction of the top wall, the light fluid finally moved to the far heated wall region. Therefore, in this region, stratification is formed in the vertical direction. The ρ distributions of THC and NGC are similar in the heating direction. For these two cases, strong stratification can be found in the vertical direction with the formation of the thermal boundary layer. The only difference is that the ρ isoline of the NGC has a slight tendency to increase.

A large ρ gradient may lead to a strong secondary flow, which in turn influences the ρ distribution. To quantitatively evaluate the magnitude of the secondary flow, the absolute velocity of the secondary flow u_{sec} is defined as:

$$u_{sec} = \sqrt{u_x^2 + u_y^2} \tag{21}$$

Fig. 6(a) shows the u_{sec} at different cross-sections for BHC and SHC. As the u_{sec} of THC and NGC are too small (less than 0.01 m · s^{-1}), they are not presented here. The streamlines of the typical cross section at $D_z = 0.3$ m for BHC and SHC are also presented in Fig. 6(b).

For the BHC, the large u_{sec} area is centralized in the center and two sides of the cross section, which are the narrow paths of the lightweight fluid leaving the heated wall, as shown in Fig. 6(b). Because the upward movement of the lightweight fluid can push the heavy fluid at the top, the heavy fluid will subsequently move towards the heated wall, which then leads to the enhancement of convection. With an increase in D_z, the secondary flow gradually disappears owing to the decrease in the density gradient, as shown in Fig. 5(c).

For the SHC, a large u_{sec} area is centralized on the heated wall and part of the top wall. With the heating of the heated wall, the lightweight fluid moves along the heated wall and reaches the top wall. Owing to the obstruction of the top wall, a lightweight fluid then changes its direction of movement from vertical to horizontal and moves along the top wall. Finally, a large vortex is formed in the cross-section, as shown in Fig. 6(b), and the overall convection is enhanced. Meanwhile, an obvious flow dead zone can be found in the top-left corner owing to the boundary friction.

Compared with the u_{sec} of BHC and SHC, the u_{sec} of THC and NGC only have small magnitudes, which can be neglected. As mentioned previously, a large ρ gradient is necessary for secondary flow. However, according to Fig. 5(b) and (c), these two cases have lowest γ_ρ and largest gradient of ρ. The presence of a ρ gradient does not ensure the existence of a secondary flow. To form a strong secondary flow, it is still needed that ρ decreases in the direction of the gravitational force.

3.2. Bulk and wall temperatures

The bulk temperature T_b and wall temperature T_w intuitively reflect the performance of active cooling. Therefore, this section analyzes T_b and T_w distributions in different cases. The average T_b was calculated using Eq. (22):

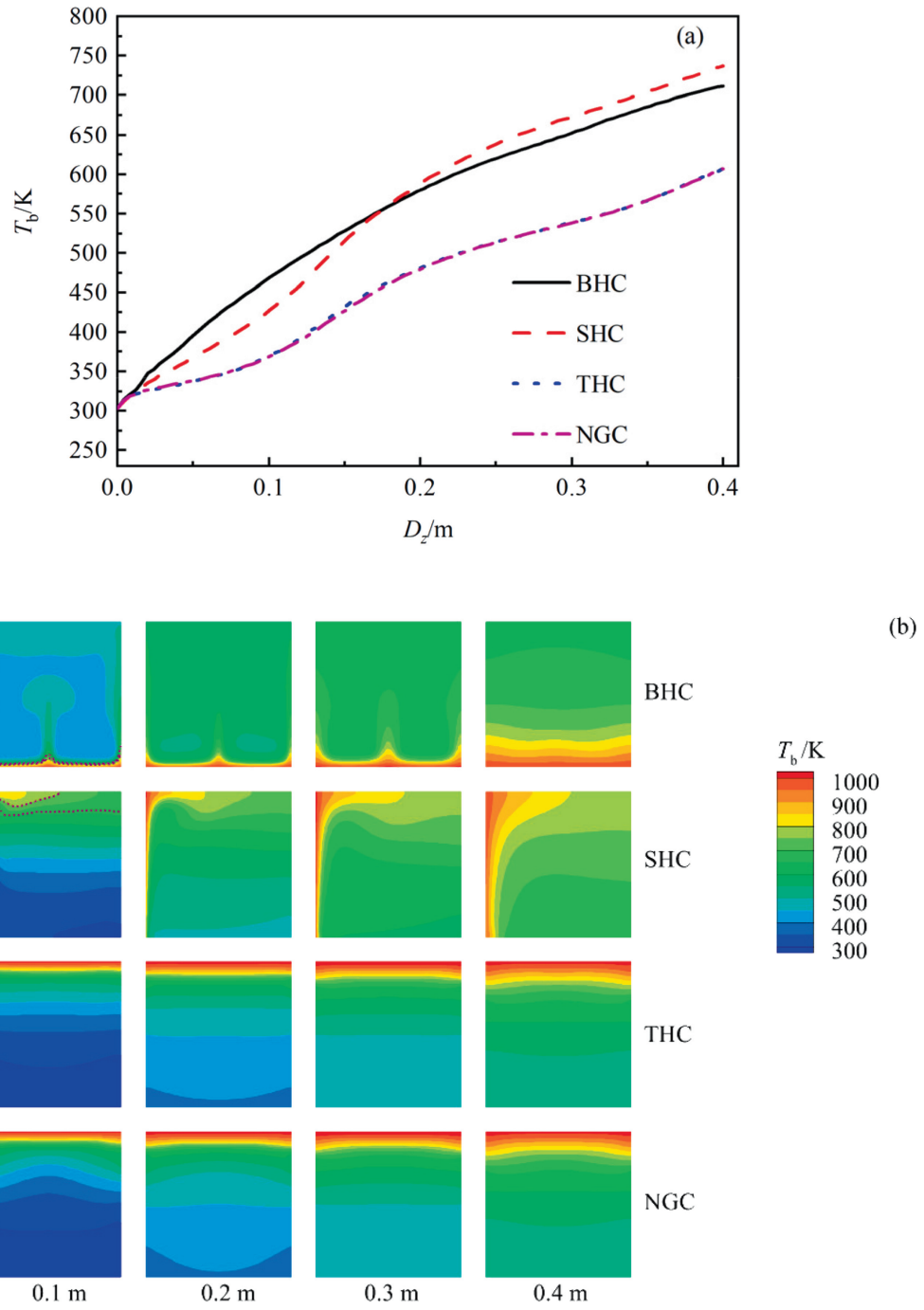

Fig. 7. (a) Bulk temperature along the channel with different heated surfaces; (b) Bulk temperature contours at different cross section with different heated surfaces.

$$T_{b,ave} = \frac{\int T_b \rho dA}{\int \rho dA} \tag{22}$$

According to T_b distribution along the cooling channel, as shown in Fig. 7(a), it was found that BHC and SHC have larger T_b values than THC and NGC. For BHC, the increase in T_b gradually becomes slower with an increase in D_z. SHC has an S-type T_b distribution, which increases slightly at the beginning and end sections and increases rapidly in the middle section. An intersection of T_b between BHC and SHC exists at approximately $D_z = 0.17$ m. THC and NGC have similar T_b distribution along the channel, which also have S-type distribution, but their variation is relatively small.

To reveal the cause of the difference in T_b distribution for these four cases, the temperature contours at different cross sections are presented in Fig. 7(b).

For THC and NGC, a significant high-temperature region can be found in the near-heated-wall region because of the relatively lower u_{sec} as shown in Fig. 6. In this high-temperature region, according to Eq. (7), the rate constant of cracking reaction can significantly increase and therefore a strong cracking reaction can occur. As the cracking reaction is an endothermic reaction, the heat from the heated wall can be effectively converted to chemical latent heat. As a result of the heat conversion, the T_b of THC and NGC is lower than that of BHC and SHC alone for the whole channel.

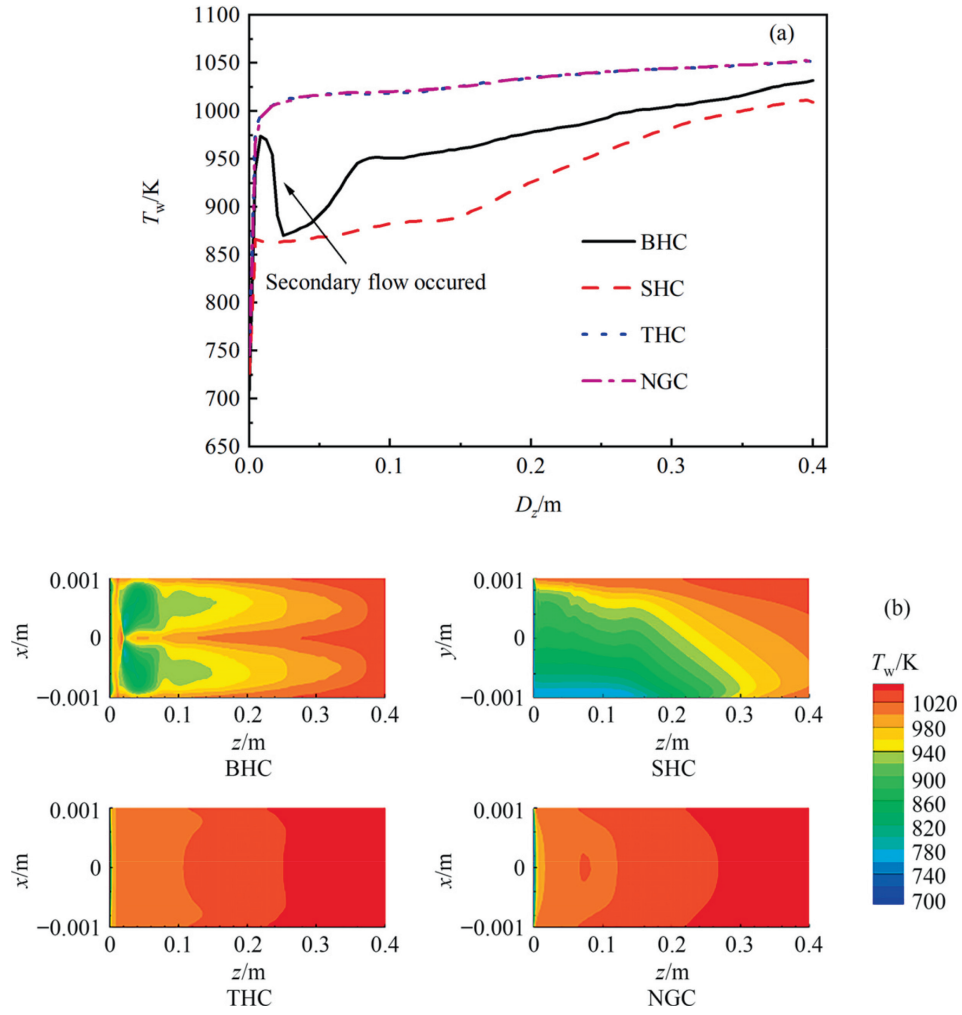

Fig. 8. (a) Wall temperature along the channel with different heated surfaces; (b) Wall temperature contours with different heated surfaces.

Both BHC and SHC exhibit obvious temperature stratification in gravitational direction alone the cooling channel. For BHC, however, this stratification diminished with an increase in D_z. At the front of the cooling channel, as most of the fluid enters the pseudo-critical region (profiled by a dashed line), the increase in T_b of SHC is inhibited by the increase in specific heat capacity. Meanwhile, with the decrease of u_{sec} in the back section, significant cracking reactions occurred and the increase in T_b for the BHC is inhibited. Therefore, an intersection of BHC and SHC T_b distribution can be found in Fig. 7(a).

The final purpose of active cooling is to reduce the wall temperature T_w. Thus, the wall temperature is a crucial index for evaluating the performance of cooling and is discussed in this section. The average wall temperature along the cooling channel was calculated using Eq. (23):

$$T_{w,ave} = \frac{\int T_w dl}{\int dl} \tag{23}$$

where l indicates the line on the heated wall and is vertical to the z-axis.

For all cases, because of the formation of a thermal boundary layer, a dramatic increase in the wall temperature can be seen at the entrance. Owing to the poor magnitude of the secondary flow, as shown in Fig. 8(a), the THC and NGC had the highest wall temperature. Meanwhile, SHC, where the cold fluid can effectively flow through the heated wall, has the lowest wall temperature. The BHC has a moderate T_w, and a sudden decrease in T_w can be observed at approximately $D_z = 0.01$ m. This drop is caused by the initiation of secondary flow. While the secondary flow is initialized, the cold fluid can enter the heated wall and then significantly decrease its temperature. As shown in Fig. 8(b), as no obvious secondary flow occurred in the heating direction, the wall temperature distributions of the THC and NGC were uniform at the cross section. Conversely, for the BHC and SHC, owing to the motion of the fluid in the heating direction, a large variation in wall temperature exists at the cross section.

For the BHC, the temperature in the center and two sides of the heated wall are much higher than those in the other positions. This is because the lightweight fluid, which has a high temperature, mainly leaves the heated wall from the center and two sides. Meanwhile, the heavy fluid, which can effectively cool the heated wall, moves towards the heated wall from another position. With the increase in D_z, owing to the elimination of secondary flow, a significant difference in the wall temperature finally disappeared at the end of the channel.

For the SHC, an obvious temperature gradient in the vertical direction can be observed from the front to the end of the channel. This phenomenon is caused by the upward motion of the fluid with light weight and high temperature. Owing to the entrance of the cold fluid, a low-temperature zone can be found at the bottom of

the heated wall. Meanwhile, owing to the dead zone shown in Fig. 6, a high temperature can be found at the top of the heated wall as well.

3.3. Energy conversion

As the thermal environment of a scramjet is severe, the local temperature in the cooling channel usually reaches the cracking temperature of the hydrocarbon fuel. Therefore, the cracking reaction can occur, and the sensible heat from the heated wall can be partly converted to chemical latent heat at these positions [3]. This energy conversion process is the core of hydrocarbon-fueled active cooling and is analyzed in detail in this section.

To acquire the reaction characteristics in the cooling channel, the average conversion is defined as Eq. (24):

$$\alpha_{ave} = \frac{\int \alpha \rho \mathrm{d}A}{\int \rho \mathrm{d}A} \tag{24}$$

The conversion distributions of THC and NGC were similar in the flow direction, as shown in Fig. 9. These two cases have the highest conversion as they have the highest wall temperatures, which can lead to the highest reaction rate in the near-heated-wall region according to Eq. (7). The BHC and SHC have similar distribution of conversion at the front section for $D_z < 0.17$ m. However, with the increase of D_z, more *n*-decane of BHC was reacted because of the higher wall temperature as shown in Fig. 8(a).

To reveal the cause of the difference, the reaction details, especially in the cross-section, need to be further characterized. Therefore, basic reaction parameters such as the mass fraction of *n*-decane $W_{C_{10}H_{22}}$, molar concentration of *n*-decane $C_{C_{10}H_{22}}$, rate constant k, and reaction rate of *n*-decane $r_{C_{10}H_{22}}$ at a typical cross section of $D_z = 0.3$ m were extracted and analyzed to further understand the energy conversion process. The distributions of these parameters along the heating direction were calculated using Eqs. (25) and (26):

$$\varphi_{ave} = \frac{\int \varphi \mathrm{d}l}{\int \mathrm{d}l} (\varphi = C, r, q) \tag{25}$$

$$\varphi_{ave} = \frac{\int \varphi \rho \mathrm{d}l}{\int \rho \mathrm{d}l} (\varphi = W, k) \tag{26}$$

where l indicates the length along the heating direction.

In the heating direction, as shown in Fig. 10, the variation in $W_{C_{10}H_{22}}$ was small, especially for BHC and SHC. For BHC and SHC, the maximum relative difference in $W_{C_{10}H_{22}}$ were only 2.6% and 2.0%, respectively. For the THC and NGC, the radial distribution of

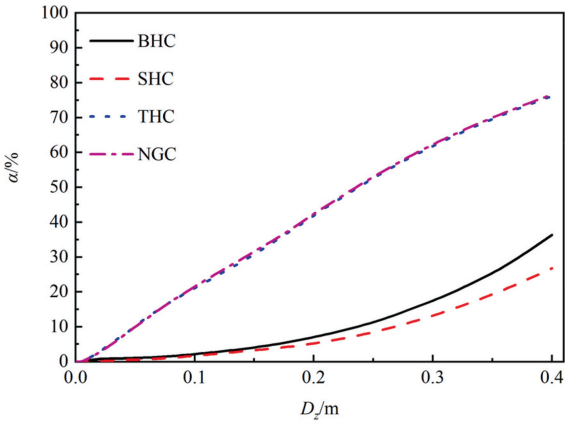

Fig. 9. Conversion of $C_{10}H_{22}$ along the channel with different heated surface.

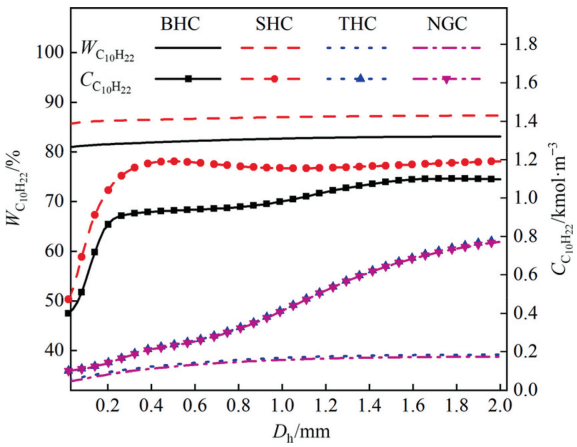

Fig. 10. Mass fraction and molar concentration of $C_{10}H_{22}$ along heating direction at the cross section of 0.3 m.

$W_{C_{10}H_{22}}$ increased slightly, but the relative differences were still less than 13.0%. This result indicates that the diffusion of *n*-decane is a quick process, which can keep $W_{C_{10}H_{22}}$ approximately uniform in the cross section.

$$C_i = \frac{W_i \rho}{M_i} \tag{27}$$

However, unlike the variation of $W_{C_{10}H_{22}}$, the variation in $C_{C_{10}H_{22}}$ is quite large in the heating direction, as shown in Fig. 10. The maximum relative differences in molar concentration in the heating direction for BHC, SHC, THC, and NGC were 188.3%, 169.7%, 681.9%, and 684.0%, respectively, which may induce significant differences in the reactions. According to Eq. (27), this phenomenon is mainly caused by the large variation in density, as shown in Fig. 5 (c), while the variation of $W_{C_{10}H_{22}}$ is small and the $M_{C_{10}H_{22}}$ is constant.

In addition to $C_{C_{10}H_{22}}$, according to Eq. (6), the rate constant k also plays a very important role in the energy conversion process. As shown in Fig. 11(b), because k is directly related to the temperature, the THC and NGC have the highest k, and SHC has the lowest k. Moreover, for all four cases, because of the rapid decrease in temperature, the rate constant k can decrease sharply in the near-heated-wall region and reach zero at approximately $D_h = 0.15$ mm. In other words, the cracking reaction only occurs in the small near-heated-wall region instead of the entire area of the cross section.

All of the above parameters jointly determine the reaction rate of *n*-decane $r_{C_{10}H_{22}}$. As shown in Fig. 11(b), in the heated wall, BHC has the highest $r_{C_{10}H_{22}}$ and the $r_{C_{10}H_{22}}$ values for the other three cases are nearly the same. With the increase of D_h, for all cases, $r_{C_{10}H_{22}}$ decreases sharply and finally reach to approximately zero at $D_h = 0.15$ mm as well as the k. From heated wall to no reaction position of $D_h = 0.15$ mm, SHC, which has the lowest reaction extent as shown in Fig. 9, always has the lowest $r_{C_{10}H_{22}}$. Meanwhile, although the BHC has the highest $r_{C_{10}H_{22}}$ in the heated wall, it decreases more sharply than the other three cases and finally is lower than THC and NGC at $D_h = 0.02$ mm. THC and NGC have similar distributions of $r_{C_{10}H_{22}}$ and their $r_{C_{10}H_{22}}$ both remain at a relatively high level.

In conclusion, the secondary flow that significantly decreases the wall temperature can also inhibit the cracking reaction. In engineering design, it is very important to find a balance that can satisfy the sufficient utilization of chemical heat absorption and the temperature limitation of the wall material.

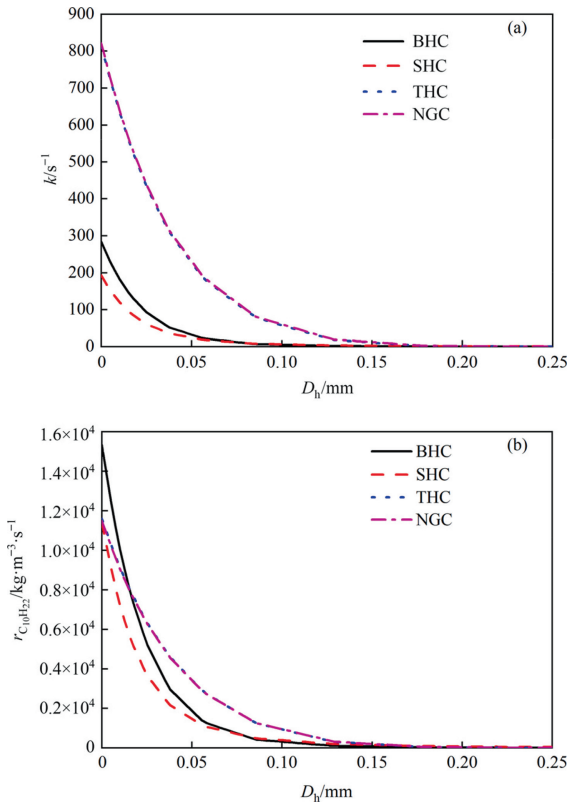

Fig. 11. (a) Rate constant and (b) reaction rate of $C_{10}H_{22}$ along heating direction at the cross section of $D_z = 0.3$ m.

3.4. Energy transport

Enhancing energy transport is an important method to improve the performance of active cooling. This process includes not only energy transport in the form of sensible heat, but also energy transport in the form of latent heat, such as chemical energy. As mentioned previously, the buoyancy effect has a significant impact on the property distribution and reaction characteristics of the fluid, which can further influence the energy transport. Therefore, understanding the effect of buoyancy on energy transport is necessary before the corresponding enhancement measures are adopted.

To reveal the underlying mechanism of energy transport, a more delicate method of analysis was established. According to the energy equation in Eq. (3), the energy transport in the cross section can be classified into four types of convection, laminar conduction, turbulence and species diffusion. To further quantitatively evaluate the contribution of these ways to the energy transfer, the equivalent heat flux (EHF) of these four ways can be defined as:

● Convection heat flux q_{conv}:

$$q_{conv} = u_h(\rho E + p) \tag{28}$$

E is the total energy of fluid:

$$E = H - \frac{p}{\rho} + \frac{\boldsymbol{U}^2}{2} \tag{29}$$

H is the sensible enthalpy:

$$H = \sum_i W_i H_i \tag{30}$$

● Laminar conduction heat flux q_{lam}:

$$q_{lam} = -\lambda_{lam}\frac{\partial T}{\partial D_h} \tag{31}$$

● Turbulence heat flux q_{tur}:

$$q_{tur} = -\lambda_{tur}\frac{\partial T}{\partial D_h} \tag{32}$$

where λ_{tur} is turbulent thermal conductivity defined in Ref. [36].

● Species diffusion heat flux q_{spec}:

$$q_{spec} = \sum_i h_i J_{i,h} \tag{33}$$

$J_{i,h}$ is the mass flux of species i in heating direction:

$$J_{i,h} = -\rho\Gamma_{eff}\frac{\partial W_i}{\partial D_h} \tag{34}$$

The total heat flux is the sum of these terms:

$$q_{tot} = q_{conv} + q_{lam} + q_{tur} + q_{spec} \tag{35}$$

As shown in Fig. 12, according to the distribution of EHFs, the cross section can be classified into three regions: near-wall region I, transition region II, and far-from-wall region III.

In near-wall region I, for all cases, q_{tot} is approximately equal to q_{lam}, and the EHFs of the other three ways are close to zero. This is because molecular motion plays a dominant role in the energy transport in the boundary layer. At the heated wall, where there is no macro flow, and only molecular diffusion exists, q_{lam} is equal to the boundary heat flux of 1.0 MW · m^{-2}. With an increase in D_h, q_{tot} decreases rapidly owing to the temperature increase and strong cracking reaction in the near-wall region.

In transition region II, for all cases, q_{lam} gradually decreases to zero, and the other ways begin to take their effect. For the BHC, q_{conv}, q_{tur} and q_{spec} rapidly increase at the beginning of region II because of the initiation of secondary flow, an increase in turbulence, and an increase in the concentration gradient. Thereafter, q_{tur} rapidly decreases to zero, as strong convection eliminates the temperature gradient. For the SHC, q_{conv} and q_{tur} rapidly increase at the beginning of region II, and then q_{tur}, as well as the BHC, quickly decrease to zero. The q_{conv} and q_{tur} of the SHC are larger than those of the BHC, and the q_{spec} of the SHC is relatively small. The EHF distributions of THC and NGC are similar. q_{tur} increases rapidly at the beginning of region II, and q_{spec} follows. Moreover, for THC and NGC, it is intriguingly noteworthy that q_{conv} has a negative value in region II. This phenomenon is caused by the reverse flow, in the direction opposite to that of heating. This negative q_{conv} indicates that convection impairs the energy transport for THC and NGC. Meanwhile, in region II, the q_{tot} of THC and NGC is less than the q_{tot} of BHC and SHC, as more heat flux was converted to chemical latent heat.

In distal region III, for all cases, q_{lam} is close to zero. In this region, convection plays a dominant role in the BHC and SHC, and turbulence plays a dominant role in the THC and NGC. For BHC and SHC, species diffusion only has a small contribution, and turbulence has almost no contribution to energy transport. For THC and NGC, convection and species diffusion both have non-negligible contributions to energy transport. It is interesting that for SHC, q_{tot} is equal to q_{tur} because the effects of convection and species diffusion offset each other. The negative q_{tur} is caused by the positive temperature gradient, as shown in Fig. 7(b). Because of this positive temperature gradient, energy can be transferred in the inverse direction of heating.

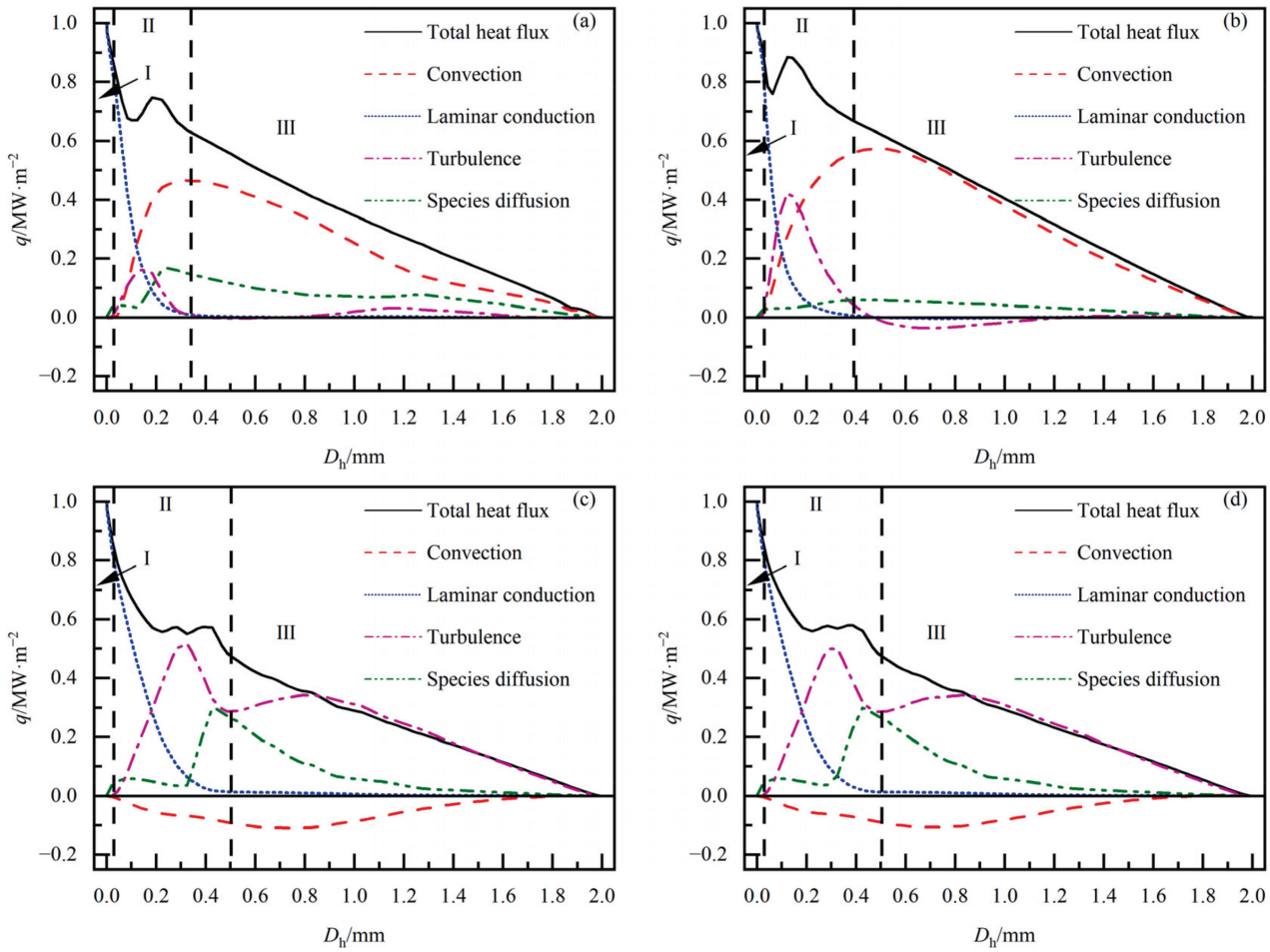

Fig. 12. Equivalent heat flux of convection, laminar conduction, turbulence and species diffusion along heating direction at cross section of $D_z = 0.3$ m with different heated walls: (a) BHC; (b) SHC; (c) THC; (d) NGC.

4. Conclusions

In the active cooling process, the buoyancy and cracking reactions are strongly coupled. Most of the previous studies have only investigated the effect of one of these phenomena; however, few studies have been conducted to determine their coupling relationship. This study numerically investigated their relationship with complete consideration of different cases of heating, and in terms of energy conversion and transport. The bottom heated case (BHC), side heated case (SHC), and top heated case (THC) were all examined and compared with the no-gravity case (NGC). The main conclusions are summarized as follows:

(1) For all cases, buoyancy had little effect on the average density distribution in the flow direction, but had a significant effect on the density profile in the cross section. For these two cases of BHC and SHC, buoyancy induced a strong secondary flow and improved the density uniformity in the cross section. Moreover, because of the buoyancy effect, for BHC and SHC, obvious density stratification occurred in the gravitational direction.

(2) The average bulk temperatures of the BHC and SHC were significantly larger than those of the THC and NGC. However, as the secondary flow enhances the heat transfer between the heated wall and fluid, the wall temperatures of the BHC and SHC were lower than those of the THC and NGC. For the wall temperature profile, the high-temperature region is positioned at the center and two sides of the heated wall for the BHC, and the top for the SHC, while the wall temperatures of the THC and NGC are uniform.

(3) The buoyancy effect can impair energy conversion by decreasing the reaction rate. At the outlet, the conversion of THC and NGC was approximately 40 % higher than that of BHC, and 50 % higher than that of SHC.

(4) According to the energy transport ways, the cross-section of the bulk fluid can be classified into three regions in the heating direction. In near-wall region I, laminar conduction plays a dominant role in all cases. In transition region II, the contribution of laminar conduction reaches zero, and the other three methods start to take their effect. Convection has a positive effect on energy transport for BHC and SHC, but has a negative effect on THC and NGC. The effect of species diffusion for THC and NGC is much greater than that for BHC and SHC. In far-from-wall region III, convection plays a dominant role for BHC and SHC, and turbulence plays a dominant role in THC and NGC.

Data Availability

Data will be made available on request.

Declaration of Competing Interest

The authors declare that they have no known competing financial interests or personal relationships that could have appeared to influence the work reported in this paper.

Acknowledgements

This work was supported by the Scientific Research Start-up Funds for Introducing Talent at Sichuan University (20822041C4013).

Nomenclature

A	area, m^2
A_0	pre-exponential factor, s^{-1}
C	molar concentration, $kmol \cdot m^{-3}$
D	distance, m
E	total energy, $J \cdot kg^{-1}$
E_a	activation energy, $kJ \cdot mol^{-1}$
g	gravity acceleration, $m \cdot s^{-2}$
H	enthalpy, $J \cdot kg^{-1}$
$\boldsymbol{J}$	mass diffusion flux, $kg \cdot m^{-2} \cdot s^{-1}$
k	rate constant, s^{-1}
l	length, m
M_w	molecular weight, $kg \cdot kmol^{-1}$
$\dot{m}$	mass flow rate, $kg \cdot s^{-1}$
p	pressure, Pa
q	heat flux, $W \cdot m^{-2}$
$\dot{q}$	volumetric heating power,$W \cdot m^{-3}$
R	universal gas constant, $J \cdot kmol^{-1} \cdot K^{-1}$
r	reaction rate, $kg \cdot m^{-3} \cdot s^{-1}$
Re	Reynolds number
T	temperature, K
$\boldsymbol{U}$	vector velocity, $m \cdot s^{-1}$
u	scalar velocity, $m \cdot s^{-1}$
V	specific volume, $m^3 \cdot kg^{-1}$
ν	stoichiometric number
W	mass fraction
x	molar fraction
α	conversion
Γ	mass diffusivity, $m^2 \cdot s^{-1}$
λ	thermal conductivity, $W \cdot m^{-1} \cdot K^{-1}$
ρ	density, $kg \cdot m^{-3}$
τ	stress tensor, $N \cdot m^{-2}$
φ	generic variable
ω	acentric factor

References

[1] E. Paquette, Cooled CMC Structures for Scramjet Engine Flowpath Components, In: 13th International Space Planes and Hypersonics Systems and Technologies Conference, Capua, Italy (2005).
[2] T.A. Jackson, D.R. Eklund, A.J. Fink, High speed propulsion: Performance advantage of advanced materials, *J. Mater. Sci.* 39 (19) (2004) 5905–5913.
[3] O.A. Powell, J.T. Edwards, R.B. Norris, K.E. Numbers, J.A. Pearce, Development of hydrocarbon-fueled scramjet engines: The hypersonic technology (H_yTech) program, *J. Propuls. Power* 17 (6) (2001) 1170–1176.
[4] S.L. Zhang, X. Li, J.Y. Zuo, J. Qin, K.L. Cheng, Y. Feng, W. Bao, Research progress on active thermal protection for hypersonic vehicles, *Prog. Aerosp. Sci.* 119 (2020) 100646.
[5] A. Chen, L. Dang, Characterization of supercritical JP-7's heat transfer and coking properties, In: 40th AIAA Aerospace Sciences Meeting & Exhibit, Reno, NV. Reston (2002).
[6] C. Liang, Y. Wang, S.C. Jiang, Q.Y. Zhang, X.Y. Li, The comprehensive study on hydrocarbon fuel pyrolysis and heat transfer characteristics, *Appl. Therm. Eng.* 117 (2017) 652–658.
[7] P.X. Jiang, J.J. Yan, S. Yan, Z.L. Lu, Y.H. Zhu, Thermal cracking and heat transfer of hydrocarbon fuels at supercritical pressures in vertical tubes, *Heat Transf. Eng.* 40 (5–6) (2019) 437–449.
[8] C.G. Yang, Z.J. Quan, Y. Chen, Q. Zhu, J.L. Wang, X.Y. Li, A comprehensive investigation of the pyrolysis effect on heat transfer characteristics for *n*-decane in the horizon mini-channel, *Energy Fuels* 34 (1) (2020) 199–210.
[9] Z.J. Jia, H.Y. Huang, W.X. Zhou, F. Qi, M.R. Zeng, Experimental and modeling investigation of *n*-decane pyrolysis at supercritical pressures, *Energy Fuels* 28 (9) (2014) 6019–6028.
[10] T.A. Ward, J.S. Ervin, R.C. Striebich, S. Zabarnick, Simulations of flowing mildly-cracked normal alkanes incorporating proportional product distributions, *J. Propuls. Power* 20 (3) (2004) 394–402.
[11] T.A. Ward, J.S. Ervin, S. Zabarnick, L. Shafer, Pressure effects on flowing mildly-cracked *n*-decane, *J. Propuls. Power* 21 (2) (2005) 344–355.
[12] J. Qin, S.L. Zhang, W. Bao, W.X. Zhou, D.R. Yu, Thermal management method of fuel in advanced aeroengines, *Energy* 49 (2013) 459–468.
[13] Y.H. Zhu, B. Liu, P.X. Jiang, Experimental and numerical investigations on *n*-decane thermal cracking at supercritical pressures in a vertical tube, *Energy Fuels* 28 (1) (2014) 466–474.
[14] H. Zhou, X.K. Gao, P.H. Liu, Q. Zhu, J.L. Wang, X.Y. Li, Energy absorption and reaction mechanism for thermal pyrolysis of *n*-decane under supercritical pressure, *Appl. Therm. Eng.* 112 (2017) 403–412.
[15] P.H. Liu, T.H. Zhang, L.X. Zhou, Z.C. Chen, Q. Zhu, J.L. Wang, X.Y. Li, Experimental and numerical analysis on flow characteristics and pyrolysis mechanism of hydrocarbon fuel with a novel online hybrid method, *Energy Convers. Manag.* 198 (2019) 111817.
[16] R.P. Jiang, G.Z. Liu, X.W. Zhang, Thermal cracking of hydrocarbon aviation fuels in regenerative cooling microchannels, *Energy Fuels* 27 (5) (2013) 2563–2577.
[17] Y. Wang, Y. Zhao, C. Liang, Y. Chen, Q.Y. Zhang, X.Y. Li, Molecular-level modeling investigation of *n*-decane pyrolysis at high temperature, *J. Anal. Appl. Pyrolysis* 128 (2017) 412–422.
[18] Z.Z. Li, H.Y. Wang, K. Jing, L.M. Wang, Y. Li, X.W. Zhang, G.Z. Liu, Kinetics and modeling of supercritical pyrolysis of endothermic hydrocarbon fuels in regenerative cooling channels, *Chem. Eng. Sci.* 207 (2019) 202–214.
[19] W.L. Yu, W.X. Zhou, L. Long, Z.J. Jia, Y.T. He, Effects of different simulation models on pyrolysis performance predictions for regenerative cooling applications, *J. Anal. Appl. Pyrolysis* 156 (2021) 105136.
[20] W. Bao, S.L. Zhang, J. Qin, W.X. Zhou, K.L. Xie, Numerical analysis of flowing cracked hydrocarbon fuel inside cooling channels in view of thermal management, *Energy* 67 (2014) 149–161.
[21] K.K. Xu, H. Meng, Modeling and simulation of supercritical-pressure turbulent heat transfer of aviation kerosene with detailed pyrolytic chemical reactions, *Energy Fuels* 29 (7) (2015) 4137–4149.
[22] Y. Feng, S.L. Zhang, J. Cao, J. Qin, Y. Cao, H.Y. Huang, Coupling relationship analysis between flow and pyrolysis reaction of endothermic hydrocarbon fuel in view of characteristic time correlation in mini-channel, *Appl. Therm. Eng.* 102 (2016) 661–671.
[23] Y. Feng, Y.G. Jiang, X. Li, S.L. Zhang, J. Qin, Y. Cao, H.Y. Huang, Numerical study on the influences of heat and mass transfers on the pyrolysis of hydrocarbon fuel in mini-channel, *Appl. Therm. Eng.* 119 (2017) 650–658.
[24] Z.Z. Li, Y. Li, X.W. Zhang, G.Z. Liu, Coupling of pyrolysis and heat transfer of supercritical hydrocarbon fuel in rectangular minichannels, *Chem. Eng. Sci.* 247 (2022) 116924.
[25] G.Z. Zhao, W.Y. Song, R.L. Zhang, Effect of pressure on thermal cracking of China RP-3 aviation kerosene under supercritical conditions, *Int. J. Heat Mass Transf.* 84 (2015) 625–632.
[26] X. Li, S.L. Zhang, M. Ye, J. Qin, W. Bao, N.G. Cui, X.Y. Liu, C.Y. Zhou, Effect of enhanced heat transfer structures on the chemical recuperation process of advanced aero-engine, *Energy* 211 (2020) 118580.
[27] Y. Feng, Y. Cao, S.Y. Liu, J. Qin, A.A. Hemeda, Y.B. Ma, The influence of coking on heat transfer in turbulent reacting flow of supercritical hydrocarbon fuels, *Int. J. Heat Mass Transf.* 144 (2019) 118623.
[28] Y. Chen, Z.L. Lei, T.H. Zhang, Q. Zhu, Z.W. Bao, Q.Y. Zhang, X.Y. Li, Flow distribution of hydrocarbon fuel in parallel minichannels heat exchanger, *AIChE J.* 64 (7) (2018) 2781–2791.
[29] Y. Chen, B. Liu, Z.L. Lei, Q.Y. Zhang, Q. Zhu, Z.W. Bao, X.Y. Li, A control method for flow distribution in fuel-cooled plate based on choked flow effect, *Appl. Therm. Eng.* 142 (2018) 127–137.
[30] J.Q. Zhu, K.H. Tao, Z. Tao, L. Qiu, Heat transfer degradation of buoyancy involved convective RP-3 hydrocarbon fuel in vertical tubes with various diameters under supercritical pressure, *Appl. Therm. Eng.* 163 (2019) 114392.
[31] X. Sun, H. Meng, Large eddy simulations and analyses of hydrocarbon fuel heat transfer in vertical upward flows at supercritical pressures, *Int. J. Heat Mass Transf.* 170 (2021) 120988.
[32] X. Sun, H. Meng, Y. Zheng, Asymmetric heating and buoyancy effects on heat transfer of hydrocarbon fuel in a horizontal square channel at supercritical pressures, *Aerosp. Sci. Technol.* 93 (2019) 105358.
[33] F. Sun, Y. Li, B. Sunden, G.N. Xie, The transport and thermodynamic characteristics of thermally oscillating phenomena in a buoyancy-driven supercritical fuel flow, *Int. J. Therm. Sci.* 159 (2021) 106550.
[34] K.K. Xu, X. Sun, H. Meng, Conjugate heat transfer, endothermic fuel pyrolysis and surface coking of aviation kerosene in ribbed tube at supercritical pressure, *Int. J. Therm. Sci.* 132 (2018) 209–218.
[35] K.K. Xu, B. Ruan, H. Meng, Validation and analyses of RANS CFD models for turbulent heat transfer of hydrocarbon fuels at supercritical pressures, *Int. J. Therm. Sci.* 124 (2018) 212–226.
[36] F.R. Menter, Two-equation eddy-viscosity turbulence models for engineering applications, *AIAA J.* 32 (8) (1994) 1598–1605.
[37] D.Y. Peng, D.B. Robinson, A new two-constant equation of state, *Ind. Eng. Chem. Fund.* 15 (1) (1976) 59–64.
[38] T.H. Chung, M. Ajlan, L.L. Lee, K.E. Starling, Generalized multiparameter correlation for nonpolar and polar fluid transport properties, *Ind. Eng. Chem. Res.* 27 (4) (1988) 671–679.

[39] E.N. Fuller, K. Ensley, J.C. Giddings, Diffusion of halogenated hydrocarbons in helium. The effect of structure on collision cross sections, *J. Phys. Chem.* 73 (11) (1969) 3679–3685.
[40] S. Takahashi, Preparation of a generalized chart for the diffusion coefficients of gases at high pressures, *J. Chem. Eng. Japan* 7 (6) (1975) 417–420.
[41] T.R. Marrero, E.A. Mason, Gaseous diffusion coefficients, *J. Phys. Chem. Ref. Data* 1 (1) (1972) 3–118.
[42] B. Zappoli, D. Beysens, Y. Garrabos, Heat Transfers and Related Effects in Supercritical Fluids, Springer, Dordrecht, 2015.
[43] G. Jaeger, The Ehrenfest classification of phase transitions: Introduction and evolution, *Arch. Hist. Exact Sci.* 53 (1) (1998) 51–81.
[44] T.L. Bergman, A.S. Lavine, F.P. Incropera, D.P. Dewitt, Fundamentals of Heat and Mass Transfer, John Wiley & Sons, New York, 2018.
[45] Y.Q. Chen, Y. Li, B. Sunden, G.N. Xie, The abnormal heat transfer behavior of supercritical *n*-decane flowing in a horizontal tube under regenerative cooling for scramjet engines, *Appl. Therm. Eng.* 167 (2020) 114637.
[46] J.D. Jackson, Fluid flow and convective heat transfer to fluids at supercritical pressure, *Nucl. Eng. Des.* 264 (2013) 24–40.
[47] Y.L. Cui, New analytical method for single-phase convective heat transfer and unified mechanism analyses on buoyancy-induced supercritical convective heat transfer deterioration, *Int. J. Heat Mass Transf.* 146 (2020) 118871.